Computational Mechanics 32 (2003) 199–213 © Springer-Verlag 2003
DOI 10.1007/s00466-003-0475-7

Stochastic meshless analysis of elastic–plastic cracked structures

B. N. Rao, S. Rahman

Abstract This paper presents a stochastic mesh-free method for probabilistic fracture-mechanics analysis of nonlinear cracked structures. The method involves enriched element-free Galerkin formulation for calculating the *J*-integral; statistical models of uncertainties in load, material properties, and crack geometry; and the first-order reliability method (FORM) for predicting probabilistic fracture response and reliability of cracked structures. The sensitivity of fracture parameters with respect to crack size, required for probabilistic analysis, is calculated using a virtual crack extension technique. Numerical examples based on mode-I fracture problems have been presented to illustrate the proposed method. The results from sensitivity analysis indicate that the maximum difference between sensitivity of the *J*-integral calculated using the proposed method and reference solutions obtained by the finite-difference method is about three percent. The results from reliability analysis show that the probability of fracture initiation using the proposed sensitivity and meshless-based FORM are very accurate when compared with either the finite-element-based Monte Carlo simulation or finite-element-based FORM. Since all gradients are calculated analytically, the reliability analysis of cracks can be performed efficiently using meshless methods.

Keywords Probabilistic fracture mechanics, Mesh-free method, Element-free galerkin method, J-integral, Sensitivity of J-integral, Probability of failure

1 Introduction

Probabilistic fracture mechanics (PFM) is becoming increasingly popular for realistic evaluation of fracture response and reliability of cracked structures. The theory of fracture mechanics provides a mechanistic relationship between the maximum permissible load acting on a structural component to the size and location of a crack – either real or postulated – in that component. Probability theory determines how the uncertainties in crack size, loads, and material properties, when modeled accurately, affect the reliability of cracked structures. PFM, which blends these two theories, accounts for both mechanistic and stochastic aspects of the fracture problem, and hence, provides a more rational means to describe the actual behavior and reliability of structures than traditional deterministic methods [1].

While development is ongoing, a number of methods have been developed for estimating statistics of various fracture response and reliability. Most of these methods are based on linear-elastic fracture mechanics (LEFM) and the finite element method (FEM) that employs the stress-intensity factor (SIF) as the primary crack-driving force [1–5]. For example, using SIFs from an FEM code, Grigoriu et al. [2] applied first- and second-order reliability methods (FORM/SORM) to predict the probability of fracture initiation and a confidence interval of the direction of crack extension. The method can account for random loads, material properties, and crack geometry. However, the randomness in crack geometry was modeled by response surface approximations of SIFs as explicit functions of crack geometry. Similar response-surface-based methods involving elastic-plastic fracture mechanics and the *J*-integral-based ductile tearing theory have also appeared [6–9]. For example, a stochastic model based on an engineering approximation of the *J*-integral and FORM/SORM have been developed by Rahman and co-workers for fracture analysis of cracked tubular structures [9]. Based on this model, the probability of fracture initiation and subsequent fracture instability can be predicted under elastic–plastic conditions. The response surface approximation used in these PFM analyses significantly reduces the complexity in calculating the derivatives of the SIF or the *J*-integral. Essentially, this presents a primary rationale for successful development of FORM/SORM algorithms for probabilistic analysis of cracked structures. However, the usefulness of response-surface-based methods is limited, since they cannot be applied to general fracture-mechanics analysis. Because of the complexity in crack geometry, external loads, and material behavior, more advanced computational tools, such as FEMs or meshless methods, must be employed to provide the necessary computational framework for analysis of general cracked structures [6].

In recent years, various Galerkin-based meshless methods have been developed or investigated to solve fracture-mechanics problems without the use of a structured grid

Received: 9 December 2002 / Accepted: 16 July 2003

B. N. Rao (✉), S. Rahman
Center for Computer-Aided Design, The University of Iowa, 208 Engineering Research Facility, Iowa City, IA 52242-1000, USA
E-mail: bnrao@engineering.uiowa.edu

The authors would like to acknowledge the financial support of the U.S. National Science Foundation (NSF) under Award No. CMS-9900196. The NSF program director was Dr. Ken Chong.

[10–19]. These gridless or meshless methods employ moving least-squares (MLS) approximation of a function that permits the resultant shape functions to be constructed entirely in terms of arbitrarily placed nodes. Since no element connectivity data is required, burdensome meshing or remeshing characteristic of the FEM is avoided. By sidestepping remeshing requirements, crack-propagation analysis can be significantly simplified. However, most mesh-free development in fracture analysis to date has been focused on either deterministic [10–16] or some probabilistic [17, 18] LEFM problems. Research in nonlinear fracture mechanics using meshless methods has not been widespread and is only currently gaining attention. For probabilistic fracture, Rao and Rahman [17] and Rahman and Rao [18] recently developed a stochastic meshless method for sensitivity and reliability analyses of linear-elastic cracked structures. The method comprises an element-free Galerkin method (EFGM) as the deterministic kernel to calculate fracture response characteristics; virtual crack extension technique to calculate sensitivities; statistical models of uncertainties in load, material properties, and crack geometry; and FORM to predict probabilistic fracture response and reliability of cracked structures. More recently, Rao and Rahman [20] developed an enriched meshless method for fracture analysis of cracks in nonlinear-elastic materials. The method involves two new enriched basis functions to capture the Hutchinson–Rice–Rosengren (HRR) [21, 22] singularity field in nonlinear fracture mechanics. The boundary layer analysis indicates that the crack-tip field predicted by using these enriched basis functions matches with the theoretical solution very well in the whole region considered, whether for the near-tip asymptotic HRR field or for the far-tip elastic field. Numerical analyses of standard fracture specimens using the enriched basis functions also yield accurate estimates of the *J*-integral. However, the aforementioned method is strictly deterministic. Hence, the next stage for further development should include stochastic meshless methods that are capable of treating uncertainties in loads, material properties, and crack geometry and predicting probabilistic fracture response and reliability of nonlinear cracked structures. Such an undertaking represents a qualitatively new development, employing meshless methods to account for both probabilistic and nonlinear aspects of fracture processes. To the best knowledge of the authors, no nonlinear meshless models for PFM analysis exist in the current literature.

This paper presents a stochastic meshless method for probabilistic fracture-mechanics analysis of homogeneous, isotropic, nonlinear-elastic, two-dimensional solids, subject to mode-I loading conditions. The method involves a nonlinear EFGM formulation for calculating fracture response characteristics; a virtual crack extension technique for sensitivity analysis; statistical models of uncertainties in load, material properties, and crack geometry; and FORM for fracture reliability analysis. Enriched basis functions are employed to capture the HRR singularity field of nonlinear fracture mechanics. Two numerical examples are presented to illustrate both the sensitivity and reliability aspects of the proposed method.

2
The element-free Galerkin Method

2.1
Moving least squares and meshless shape function

Consider a function $u(\mathbf{x})$ over a domain $\Omega \subseteq \Re^2$. Let $\Omega_{\mathbf{x}} \subseteq \Omega$ denote a sub-domain describing the neighborhood of a point $\mathbf{x} \in \Re^K$ located in Ω. According to the MLS [23] method, the approximation $u^h(\mathbf{x})$ of u $(\mathbf{x})$ is

$$u^h(\mathbf{x}) = \sum_{i=1}^{m} p_i(\mathbf{x}) a_i(\mathbf{x}) = \mathbf{p}^T(\mathbf{x})\mathbf{a}(\mathbf{x}) \ , \tag{1}$$

where $\mathbf{p}^T(\mathbf{x}) = \{p_1(\mathbf{x}), \cdots, p_m(\mathbf{x})\}$ is a vector of complete basis functions of order m and $\mathbf{a}(\mathbf{x}) = \{a_1(\mathbf{x}), \ldots, a_m(\mathbf{x})\}$ is a vector of unknown parameters that depend on $\mathbf{x}$. The coefficient vector $\mathbf{a}(\mathbf{x})$ is determined by minimizing a weighted discrete L_2 norm, defined as

$$\begin{aligned} J(\mathbf{x}) &= \sum_{I=1}^{n} w_I(\mathbf{x}) \left[\mathbf{p}^T(\mathbf{x}_I)\mathbf{a}(\mathbf{x}) - d_I\right]^2 \\ &= [\mathbf{P}\mathbf{a}(\mathbf{x}) - \mathbf{d}]^T \mathbf{W} [\mathbf{P}\mathbf{a}(\mathbf{x}) - \mathbf{d}] \ , \end{aligned} \tag{2}$$

where $\mathbf{x}_I$ denotes the coordinates of node I, $\mathbf{d}^T = \{d_1, d_2, \ldots, d_n\}$ with d_I representing the nodal parameter for node I , $\mathbf{W} = \mathrm{diag}[w_1(\mathbf{x}), w_2(\mathbf{x}), \ldots, w_n(\mathbf{x})]$ with $w_I(\mathbf{x})$ being the weight function associated with node I, such that $w_I(\mathbf{x}) > 0$ for all $\mathbf{x}$ in the support $\Omega_{\mathbf{x}}$ of $w_I(\mathbf{x})$ and *zero* otherwise, n is the number of nodes in $\Omega_{\mathbf{x}}$ for which $w_I(\mathbf{x}) > 0$, and $\mathbf{P} = [\mathbf{p}^T(\mathbf{x}_1), \ldots, \mathbf{p}^T(\mathbf{x}_n)] \in L(\Re^n \times \Re^m)$. In this study, a weight function proposed by Rao and Rahman [15] was used, which is

$$w_I(\mathbf{x}) = \begin{cases} \dfrac{\left(1+\beta^2 \frac{z_I^2}{z_{mI}^2}\right)^{-\left(\frac{1+\beta}{2}\right)} - \left(1+\beta^2\right)^{-\left(\frac{1+\beta}{2}\right)}}{1-\left(1+\beta^2\right)^{-\left(\frac{1+\beta}{2}\right)}}, & z_I \le z_{mI} \\ 0, & z_I > z_{mI} \end{cases} \ , \tag{3}$$

where β is a shape controlling parameter, $z_I = \| \mathbf{x} - \mathbf{x}_\mathbf{I} \|$, and z_{mI} is the domain of influence of node I . The stationarity of $J(\mathbf{x})$ with respect to $\mathbf{a}(\mathbf{x})$ yields

$$\mathbf{A}(\mathbf{x})\mathbf{a}(\mathbf{x}) = \mathbf{C}(\mathbf{x})\mathbf{d} \ , \tag{4}$$

where

$$\mathbf{A}(\mathbf{x}) = \sum_{I=1}^{n} w_I(\mathbf{x})\mathbf{p}(\mathbf{x}_I)\mathbf{p}^T(\mathbf{x}_I) = \mathbf{P}^T\mathbf{W}\mathbf{P} \tag{5}$$

and

$$\mathbf{C}(\mathbf{x}) = [w_1(\mathbf{x})\mathbf{p}(\mathbf{x}_1), \ldots, w_n(\mathbf{x})\mathbf{p}(\mathbf{x}_n)] = \mathbf{P}^T\mathbf{W} \ . \tag{6}$$

Solving for $\mathbf{a}(\mathbf{x})$ in Eq. (4) and then substituting into Eq. (1) yields

$$u^h(\mathbf{x}) = \sum_{I=1}^{n} \Phi_I(\mathbf{x}) d_I = \mathbf{\Phi}^T(\mathbf{x})\mathbf{d} \ , \tag{7}$$

where

$$\begin{aligned} \mathbf{\Phi}^T(\mathbf{x}) &= \{\Phi_1(\mathbf{x}), \Phi_2(\mathbf{x}), \ldots \Phi_n(\mathbf{x})\} \\ &= \mathbf{p}^T(\mathbf{x})\mathbf{A}^{-1}(\mathbf{x})\mathbf{C}(\mathbf{x}) \end{aligned} \tag{8}$$

is a vector with its Ith component,

$$\mathbf{\Phi}_I(\mathbf{x}) = \sum_{j=1}^{m} p_j(\mathbf{x}) \left[\mathbf{A}^{-1}(\mathbf{x})\mathbf{C}(\mathbf{x})\right]_{jI} \ , \tag{9}$$

representing the shape function of the MLS approximation corresponding to node I. The partial derivatives of $\Phi_I(\mathbf{x})$ can also be obtained as

$$\mathbf{\Phi}_{I,i}(\mathbf{x}) = \sum_{j=1}^{m} \left\{ p_{j,i}(\mathbf{A}^{-1}\mathbf{C})_{jI} + p_j(\mathbf{A}_{,i}^{-1}\mathbf{C} + \mathbf{A}^{-1}\mathbf{C}_{,i})_{jI} \right\} \ , \tag{10}$$

where $\mathbf{A}_{,i}^{-1} = -\mathbf{A}^{-1}\mathbf{A}_{,i}\mathbf{A}^{-1}$ and $()_{,i} = \partial()/\partial x_i$.

2.2 Variational formulation and discretization

For small displacements in two-dimensional, homogeneous, isotropic solids, the equilibrium equations and boundary conditions are

$$\nabla \cdot \boldsymbol{\sigma} + \mathbf{b} = \mathbf{0} \quad \text{in} \quad \Omega \tag{11}$$

and

$$\begin{aligned} \boldsymbol{\sigma} \cdot \mathbf{n} &= \bar{\mathbf{t}} \quad \text{on} \quad \Gamma_t \ \text{(natural boundary conditions)} \\ \mathbf{u} &= \bar{\mathbf{u}} \quad \text{on} \quad \Gamma_u \ \text{(essential boundary conditions)} \end{aligned} \ , \tag{12}$$

respectively, where $\boldsymbol{\sigma}$ is the stress vector, $\boldsymbol{\epsilon} = \nabla_s \mathbf{u}$ is the strain vector, $\mathbf{u}$ is the displacement vector, $\mathbf{b}$ is the body force vector, $\bar{\mathbf{t}}$ and $\bar{\mathbf{u}}$ are the vectors of prescribed surface tractions and displacements, respectively, $\mathbf{n}$ is a unit normal to the domain, Ω, Γ_t and Γ_u are the portions of boundary Γ where tractions and displacements are prescribed, $\nabla^T = \{\partial/\partial x_1, \partial/\partial x_2\}$ is the vector of gradient operators, and $\nabla_s \mathbf{u}$ is the symmetric part of $\nabla \mathbf{u}$. The variational or weak form of Eqs. (11) and (12) is

$$\int_\Omega \boldsymbol{\sigma}^T \delta\boldsymbol{\epsilon} \, d\Omega - \int_\Omega \mathbf{b}^T \delta\mathbf{u} \, d\Omega - \int_\Omega \bar{\mathbf{t}}^T \delta\mathbf{u} \, d\Gamma + \sum_{x_K \in \Gamma_u} \mathbf{f}^T(\mathbf{x}_K)\delta\mathbf{u}(\mathbf{x}_K) + \sum_{x_K \in \Gamma_u} \delta\mathbf{f}^T(\mathbf{x}_K)[\mathbf{u}(\mathbf{x}_K) - \bar{\mathbf{u}}(\mathbf{x}_K)] = 0 \ , \tag{13}$$

where $\mathbf{f}^T(\mathbf{x}_K)$ is the vector of reaction forces at the constrained node K on Γ_u and δ denotes the variation operator. Note, Eq. (13) is nonlinear with respect to displacement $\mathbf{u}$, because of the nonlinearity in the stress–strain relationship. From Eq. (7), the MLS approximation of $\mathbf{u}(\mathbf{x}) = \{u_1(\mathbf{x}), u_2(\mathbf{x})\}^T$ in two dimensions is

$$\mathbf{u}^h(\mathbf{x}) = \mathbf{\Phi}^T \mathbf{d} \ , \tag{14}$$

where

$$\mathbf{\Phi}^T(x) = \begin{bmatrix} \Phi_1(\mathbf{x}) & 0 & \Phi_2(\mathbf{x}) & 0 & \cdots & \Phi_N(\mathbf{x}) & 0 \\ 0 & \Phi_1(\mathbf{x}) & 0 & \Phi_2(\mathbf{x}) & \cdots & 0 & \Phi_N(\mathbf{x}) \end{bmatrix} \ , \tag{15}$$

$\mathbf{d} = \{d_1^1, d_1^2, \ldots d_N^1, d_N^2\}^T \in \Re^{2N}$ is the vector of nodal parameters or generalized displacements, and N is the total number of nodal points in Ω. Applying the MLS approximation of Eq. (14) into Eq. (13) yields nonlinear algebraic equations, which must be solved by iterative methods. The standard Newton–Raphson method was used to solve these nonlinear equations, as follows.

Let $\mathbf{d}^r$ denote the nodal parameter vector at the rth iteration. Upon Taylor series expansion at $\mathbf{d}^r$ and retaining only the linear term, Eq. (13) leads to

$$\begin{bmatrix} \mathbf{k}(\mathbf{d}^r) & \mathbf{G} \\ \mathbf{G}^T & 0 \end{bmatrix} \begin{Bmatrix} \Delta\mathbf{d}^r \\ \mathbf{f}_R \end{Bmatrix} - \begin{Bmatrix} \mathbf{f}^{ext} - \mathbf{f}^{int}(\mathbf{d}^r) \\ \mathbf{g} - \mathbf{h}(\mathbf{d}^r) \end{Bmatrix} = 0 \ , \tag{16}$$

where $\Delta\mathbf{d}^r = \mathbf{d}^{r+1} - \mathbf{d}^r$ is the incremental solution,

$$\mathbf{k} = [\mathbf{k}_{IJ}^r] = \begin{bmatrix} \mathbf{k}_{11}^r & \mathbf{k}_{12}^r & \cdots & \mathbf{k}_{1N}^r \\ \mathbf{k}_{21}^r & \mathbf{k}_{22}^r & \cdots & \mathbf{k}_{2N}^r \\ \vdots & \vdots & \vdots & \vdots \\ \mathbf{k}_{N1}^r & \mathbf{k}_{N2}^r & \cdots & \mathbf{k}_{NN}^r \end{bmatrix} \in L\left(\Re^{2N} \times \Re^{2N}\right) \tag{17}$$

is the tangent stiffness matrix at $\mathbf{d}^r$ with

$$\mathbf{k}_{IJ}^r = \int_\Omega \mathbf{B}_I^T \left[\left. \frac{\partial\boldsymbol{\epsilon}}{\partial\boldsymbol{\sigma}} \right|_{d^r} \right]^{-1} \mathbf{B}_J \, d\Omega \in L\left(\Re^2 \times \Re^2\right) \ , \tag{18}$$

$$G^T = \begin{bmatrix} \Phi_1(\mathbf{x}_1) & 0 & \Phi_1(\mathbf{x}_2) & 0 & \cdots & \Phi_1(\mathbf{x}_N) & 0 \\ 0 & \Phi_1(\mathbf{x}_1) & 0 & \Phi_1(\mathbf{x}_2) & \cdots & 0 & \Phi_1(\mathbf{x}_N) \\ \Phi_2(\mathbf{x}_1) & 0 & \Phi_2(\mathbf{x}_2) & 0 & \cdots & \Phi_2(\mathbf{x}_N) & 0 \\ \cdots & \Phi_2(\mathbf{x}_1) & 0 & \Phi_2(\mathbf{x}_2) & \cdots & 0 & \Phi_2(\mathbf{x}_N) \\ \vdots & \vdots & \vdots & \vdots & \vdots & \vdots & \vdots \\ \Phi_L(\mathbf{x}_1) & 0 & \Phi_L(\mathbf{x}_2) & 0 & \cdots & \Phi_L(\mathbf{x}_N) & 0 \\ 0 & \Phi_L(\mathbf{x}_1) & 0 & \Phi_L(\mathbf{x}_2) & \cdots & 0 & \Phi_L(\mathbf{x}_N) \end{bmatrix} \in L(\Re^{2L} \times \Re^{2N}) \tag{19}$$

is a matrix comprising shape functions of L nodes at which the displacement boundary conditions are prescribed on Γ_u, $\mathbf{f}_R = \{f_1(\mathbf{x}_{K_1}), f_2(\mathbf{x}_{K_1}), \ldots f_1(\mathbf{x}_{K_L}), f_2(\mathbf{x}_{K_L})\}^T \in \Re^{2L}$ is the vector of all reaction forces on Γ_u,

$$\mathbf{f}^{ext} = \int_\Omega \mathbf{\Phi}^T \mathbf{b} \, d\Omega + \int_{\Gamma_t} \mathbf{\Phi}^T \bar{\mathbf{t}} \, d\Gamma \in \Re^{2N} \tag{20}$$

is the external force vector. Noting that $\mathbf{d}_J^r = \left\{d_{J1}^r, d_{J2}^r\right\}^T \in \Re^2$, $\mathbf{f}^{int}(\mathbf{d}^r) = \left\{\mathbf{f}_1^{int}(\mathbf{d}^r), \ldots, \mathbf{f}_N^{int}(\mathbf{d}^r)\right\}^T \in \Re^{2N}$ is the internal force vector with

$$\mathbf{f}_I^{int}(\mathbf{d}^r) = \int_\Omega \mathbf{B}_I^T \left[\frac{\partial \boldsymbol{\epsilon}}{\partial \boldsymbol{\sigma}}\bigg|_{\mathbf{d}^r}\right]^{-1} \mathbf{B}_J \mathbf{d}_J^r \, \mathrm{d}\Omega \in \Re^2 \quad , \tag{21}$$

$\mathbf{g} = \{\bar{\mathbf{u}}(\mathbf{x}_{K_1}), \ldots, \bar{\mathbf{u}}(\mathbf{x}_{K_L})\}^T \in \Re^{2L}$ is the vector of all prescribed displacements on Γ_u, $\mathbf{h}(\mathbf{d}^r) = \{\boldsymbol{\Phi}^T(\mathbf{x}_{K_1})\mathbf{d}^r, \ldots, \boldsymbol{\Phi}^T(\mathbf{x}_{K_L})\mathbf{d}^r\}^T \in \Re^{2L}$, and

$$\mathbf{B}_I = \begin{bmatrix} \Phi_{I,1} & 0 \\ 0 & \Phi_{I,2} \\ \Phi_{I,2} & \Phi_{I,1} \end{bmatrix} \quad . \tag{22}$$

Equation 16 represents a system of linear equations in $\Delta\mathbf{d}^r$ and can be easily solved using standard numerical methods. Hence, the total solution at the $(r+1)$th iteration is

$$\mathbf{d}^{r+1} = \mathbf{d}^r + \Delta\mathbf{d}^r \quad . \tag{23}$$

The iteration in Eq. (23) is continued until both convergence criteria, defined by

$$\frac{\|\Delta\mathbf{d}^r\|}{\|\mathbf{d}^{r+1}\|} \leq \varepsilon_1 \tag{24}$$

and

$$\frac{\|\Delta\mathbf{R}^r\|}{\|\mathbf{R}^{r+1}\|} \leq \varepsilon_2 \quad , \tag{25}$$

are satisfied, where $\mathbf{R}^r = \mathbf{f}^{ext} - \mathbf{f}^{int}(\mathbf{d}^r)$ is the residual at the ith iteration, $\Delta\mathbf{R}^r = \mathbf{R}^{r+1} - \mathbf{R}^r$, and ε_1 and ε_2 are the pre-selected tolerances.

To perform numerical integration in Eqs. (18), (20) and (21), a background mesh is required, which can be independent of the arrangement of the meshless nodes. However, in this study, the nodes of the background mesh coincide with the meshless nodes. Standard Gaussian quadratures were used to evaluate the integrals for assembling the stiffness matrix and the force vector. In general, a 4×4 quadrature is adequate, except in the cells surrounding a high stress gradient (e.g., near a crack tip) where a 8×8 quadrature is suggested.

In solving for $\Delta\mathbf{d}^r$, the essential boundary conditions must be enforced. The lack of Kronecker delta properties in the meshless shape functions presents some difficulty in imposing the essential boundary conditions in EFGM. Nevertheless, several methods are currently available for enforcing essential boundary conditions. A full transformation method [15, 24] was used in this work.

It should be noted that the generalized displacement vector $\mathbf{d}$ represents the nodal parameters, not the actual displacements at the meshless nodes. However, the actual displacement vector $\hat{\mathbf{d}} = \{\mathbf{u}(\mathbf{x}_1), \ldots, \mathbf{u}(\mathbf{x}_N)\}^T \in \Re^{2N}$ can be easily calculated from

$$\hat{\mathbf{d}} = \wedge\mathbf{d} \tag{26}$$

where $\wedge = [\boldsymbol{\Phi}(\mathbf{x}_1), \ldots, \boldsymbol{\Phi}(\mathbf{x}_N)]^T \in L(\Re^{2N} \times \Re^{2N})$ is the transformation matrix.

3
The *J* integral and HRR field

Consider a two-dimensional structure with a rectilinear crack of length $2a$, orientation γ, subjected to external loads, $S_1, S_2, \cdots, S_M$, as shown in Fig. 1. Under quasi-static

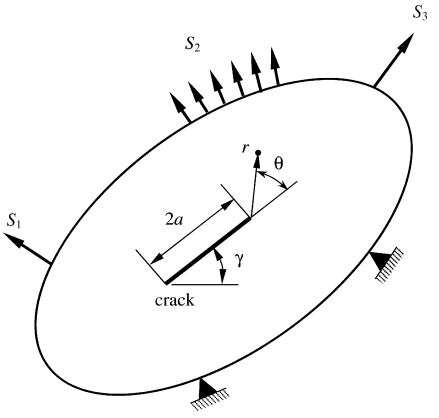

Fig. 1. A cracked structure under mixed-mode loading

condition, in the absence of body forces, thermal strains, and crack-face tractions, the domain form of the J-integral for a two-dimensional problem is

$$J = \int_A \left(\sigma_{ij}\frac{\partial u_i}{\partial x_1} - W\delta_{1j}\right)\frac{\partial q}{\partial x_j}\,\mathrm{d}A \quad , \tag{27}$$

where $W = \int \boldsymbol{\sigma}_{ij}\,\mathrm{d}\varepsilon_{ij}$ is the strain energy density, u_i and $T_i = \sigma_{ij}n_j$ are the ith component of displacement and traction vectors, A is the area inside an arbitrary contour around the crack tip, and q is a weight function that has a value of unity at the outer boundary of A and *zero* at the crack tip.

Consider a power-law hardening material with a uniaxial stress-strain $(\sigma - \varepsilon)$ relation as

$$\frac{\varepsilon}{\varepsilon_0} = \alpha\left(\frac{\sigma}{\sigma_0}\right)^n \quad , \tag{28}$$

where σ_0 is the reference stress, $\varepsilon_0 = \sigma_0/E$ is the reference strain with E representing Young's modulus, α is a material constant, and n is the material hardening exponent. When $n = 1$ and ∞, Eq. (28) represents linear-elastic and rigid-perfectly plastic materials, respectively. In reality, however, the Ramberg–Osgood law [25] is employed to describe nonlinear stress-strain curve, which is

$$\frac{\varepsilon}{\varepsilon_0} = \frac{\sigma}{\sigma_0} + \alpha\left(\frac{\sigma}{\sigma_0}\right)^n \quad . \tag{29}$$

For multiaxial stress state, the Ramberg–Osgood law can be generalized as

$$\varepsilon_{ij} = \varepsilon_{ij}^e(\sigma_{ij}) + \varepsilon_{ij}^p(\sigma_{ij}) \quad , \tag{30}$$

where

$$\varepsilon_{ij}^e = \frac{1+\nu}{E}s_{ij} + \frac{1-2\nu}{3E}\sigma_{kk}\delta_{ij} \tag{31}$$

and

$$\varepsilon_{ij}^p = \frac{3}{2}\alpha\varepsilon_0\left(\frac{\sigma_e}{\sigma_0}\right)^{n-1}\frac{s_{ij}}{\sigma_0} \tag{32}$$

are the elastic and plastic components of strain, respectively, ν is the Poisson's ratio, $s_{ij} = \sigma_{ij} - \sigma_{kk}\delta_{ij}/3$ is the deviatoric stress, $\sigma_e = \sqrt{3s_{ij}s_{ij}/2}$ is the von Mises effective

stress, and δ_{ij} is the Kronecker delta. If elastic strains are negligible compared with plastic strains (i.e., $\varepsilon_{ij} \simeq \varepsilon_{ij}^{p}$), Eq. (32) represents a pure power-law-strain-hardening material, for which the asymptotic crack-tip fields under mode-I loading are [26, 27]

$$\sigma_{ij} = \sigma_0 \left[\frac{J}{\alpha\sigma_0\varepsilon_0 I_n r}\right]^{\frac{1}{n+1}} \tilde{\sigma}_{ij}(\theta, n) \ , \tag{33}$$

$$\varepsilon_{ij} = \alpha\varepsilon_0 \left[\frac{J}{\alpha\sigma_0\varepsilon_0 I_n r}\right]^{\frac{n}{n+1}} \tilde{\varepsilon}_{ij}(\theta, n) \ , \tag{34}$$

and

$$u_i = \alpha\varepsilon_0 r \left[\frac{J}{\alpha\sigma_0\varepsilon_0 I_n r}\right]^{\frac{n}{n+1}} \tilde{u}_i(\theta, n) \ , \tag{35}$$

where r and θ are the polar coordinates with the origin at the crack tip, I_n is a dimensionless constant that depends on n, and $\tilde{\sigma}_{ij}, \tilde{\varepsilon}_{ij}$, and $\tilde{u}_i$ are dimensionless angular functions of θ and n. The parameters I_n, $\tilde{\sigma}_{ij}, \tilde{\varepsilon}_{ij}$, and $\tilde{u}_i$ also depend on the state of stress. Eqs. (33)–(35) represent the well-known HRR field under mode-I deformation [26, 27]. Note, the same HRR field also exists in mixed-mode fracture, in which case the dimensionless angular functions also depend on the magnitude of mode-mixity [28].

Although the HRR solution describes the nature of the dominant singularity, higher order terms may have an important effect on the constraint of plane strain crack-tip fields [29–32]. The HRR field is thus not the only possible crack-tip field, but should be regarded as an important limiting case of a family of fields, which arise when higher order terms are insignificant.

4
Enriched basis functions

When solving problems involving cracks, a convenient way of capturing stress-singularity at a crack tip is by using appropriately defined enriched basis functions. Existing enriched basis functions, typically used to capture the LEFM singularity [12], may not be appropriate for solving nonlinear fracture-mechanics problems. The singularity of crack-tip field in nonlinear fracture is different than that in LEFM and depends on the material hardening characteristics. In a recent study, Rao and Rahman [20] developed two new enriched basis functions for fracture analysis of cracks in nonlinear-elastic materials.

There are several ways to enrich the EFGM formulation to capture the HRR stress singularity in elastic-plastic materials. One approach involves augmenting the EFGM trial functions by the near-tip displacement field, thereby including additional unknown coefficients for each crack tip. Hence, both the stiffness matrix and the force vector need to be augmented leading to a larger system of equations. Furthermore, the computer programming can be rather involved. An alternative approach entails expanding the EFGM basis functions directly to include terms from the near-tip displacement field. The enrichment based on expanded basis functions requires simpler computer programming, but can become expensive for multiple cracks. The enrichment based on expanded basis functions was developed by Rao and Rahman [20]. In this section, both the enrichment for LEFM basis functions and the enrichment for nonlinear fracture mechanics are briefly summarized.

4.1
Linear-elastic fracture mechanics

In LEFM, the asymptotic near tip displacement field $\mathbf{u} = \{u_1, u_2\}^T$ is given by

$$u_1 = \frac{1}{\mu}\sqrt{\frac{r}{2\pi}}\left[K_I g_1^I(\theta) + K_{II} g_1^{II}(\theta)\right] \tag{36}$$

and

$$u_2 = \frac{1}{\mu}\sqrt{\frac{r}{2\pi}}\left[K_I g_2^I(\theta) + K_{II} g_2^{II}(\theta)\right] \ , \tag{37}$$

where $\mu = E/[2(1+\nu)]$ is the shear modulus,

$$\begin{aligned} g_1^I(\theta) &= \kappa - \cos\frac{\theta}{2} + \sin\theta\,\sin\frac{\theta}{2} \\ g_2^I(\theta) &= \kappa + \sin\frac{\theta}{2} - \sin\theta\,\cos\frac{\theta}{2} \\ g_1^{II}(\theta) &= \kappa + \sin\frac{\theta}{2} + \sin\theta\,\cos\frac{\theta}{2} \\ g_2^{II}(\theta) &= \kappa - \cos\frac{\theta}{2} - \sin\theta\,\sin\frac{\theta}{2} \end{aligned} \tag{38}$$

are the well-known angular functions of LEFM, K_I and K_{II} are mode-I and mode–II SIFs, and the Kolosov constant $\kappa = (3-\nu)/(1+\nu)$ for plane stress and $\kappa = 3-4\nu$ for plane stress. Using trigonometric identities, it can be shown that the basis, given by

$$\mathbf{p}^T(\mathbf{x}) = \left\{1, x_1, x_2, \sqrt{r}\cos\frac{\theta}{2}, \sqrt{r}\sin\frac{\theta}{2}, \sqrt{r}\sin\frac{\theta}{2}\sin\theta, \sqrt{r}\cos\frac{\theta}{2}\sin\theta\right\} , \tag{39}$$

spans the LEFM crack-tip displacement field in Eqs. (36) and (37) exactly [12]. Indeed, the enriched basis in Eq. (39) has been successfully used in meshless analysis of linear-elastic cracked structures [12, 15–18], including analysis of cracks in functionally graded materials [19]. However, the HRR field is different from the LEFM crack-tip field. Hence, there is a need of new basis functions for nonlinear fracture-mechanics analysis.

4.2
Nonlinear fracture mechanics

According to Eqs. (33)–(35), the HRR field is a known field. Hence, by embedding the HRR displacement field, enriched basis functions similar to Eq. (39) can be developed for its use in nonlinear fracture mechanics. However, the angular functions $\tilde{u}_i(\theta, n)$ in Eq. (35) cannot be obtained in closed-form. An eigenvalue problem needs to be solved numerically to determine $\tilde{u}_i(\theta, n)$ [33]. As an alternative, simpler functional forms that can approximate the HRR field can be potentially used to form the enriched basis.

Consider two approximations of $\tilde{u}_i(\theta, n)$, given by

Approximation I:

$$\tilde{\boldsymbol{u}}_i(\theta,n) \simeq \tilde{\boldsymbol{a}}_{0i}(n) + \tilde{\boldsymbol{a}}_{1i}(n)\cos\frac{\theta}{2} + \tilde{\boldsymbol{a}}_{2i}(n)\sin\frac{\theta}{2} + \tilde{\boldsymbol{a}}_{3i}(n)\sin\frac{\theta}{2}\sin\theta + \tilde{\boldsymbol{a}}_{4i}(n)\cos\frac{\theta}{2}\sin\theta \tag{40}$$

and

Approximation II:

$$\tilde{\boldsymbol{u}}_i(\theta,n) \simeq \tilde{\boldsymbol{a}}_{0i}(n) + \tilde{\boldsymbol{a}}_{1i}(n)\cos\frac{\theta}{2} + \tilde{\boldsymbol{a}}_{2i}(n)\sin\frac{\theta}{2} + \tilde{\boldsymbol{a}}_{3i}(n)\sin\frac{\theta}{2}\sin\theta + \tilde{\boldsymbol{a}}_{4i}(n)\cos\frac{\theta}{2}\sin\theta + \tilde{\boldsymbol{a}}_{5i}(n)\sin\frac{\theta}{2}\sin 3\theta + \tilde{\boldsymbol{a}}_{6i}(n)\cos\frac{\theta}{2}\sin 3\theta \tag{41}$$

The first equation (Eq. (40)) involves a linear combination of components of the basis function vector in Eq. (39) (minus the linear terms). The second equation (Eq. (41)) entails adding two arbitrarily chosen terms, $\sin\theta/2\sin 3\theta$ and $\cos\theta/2\sin 3\theta$, to Eq. (40) for a better approximation. To evaluate these two approximations, Shih's [33] HRR field data of $\tilde{\boldsymbol{u}}_i(\theta,n), i=1,2$, obtained by solving the eigenvalue problem numerically, were fitted with Eqs. (40) and (41). Note that Shih's [33] HRR field data was reported in polar coordinate system, so a polar to rectangular coordinate system transformation was performed before fitting the HRR data using Eqs. (40) and (41). Figure 2a shows the plots of $\tilde{\boldsymbol{u}}_i(\theta,n)$ from Eq. (40), as a function of θ for materials with high-hardening (n = 3), medium-hardening (n = 10), and low-hardening (n = 50) characteristics for the plane stress condition. The comparison with Shih's HRR field data indicates that Eq. (40), obtained from the LEFM basis function, provides a reasonably good approximation of $\tilde{\boldsymbol{u}}_i(\theta,n)$. Similar comparisons in Fig. 2b, which involve plots of Eq. (41), show slightly improved results in fitting Shih's numerical results. The above observations also hold true for the plane strain condition, the results of which are shown in Fig. 3a and 3b, involving plots of Eqs. (40) and (41), respectively. Hence, both Eq. (40) and (41) can be used to approximate $\tilde{\boldsymbol{u}}_i(\theta,n)$ for nonlinear-fracture mechanics analysis. Consequently, two types of enriched basis functions are proposed, which are

$$\text{Type I: } \mathbf{p}^T(\mathbf{x}) = \left\{1, x_1, x_2, r^{\frac{1}{n+1}}\cos\frac{\theta}{2}, r^{\frac{1}{n+1}}\sin\frac{\theta}{2}, r^{\frac{1}{n+1}} \times \sin\frac{\theta}{2}\sin\theta, r^{\frac{1}{n+1}}\cos\frac{\theta}{2}\sin\theta\right\}, \tag{42}$$

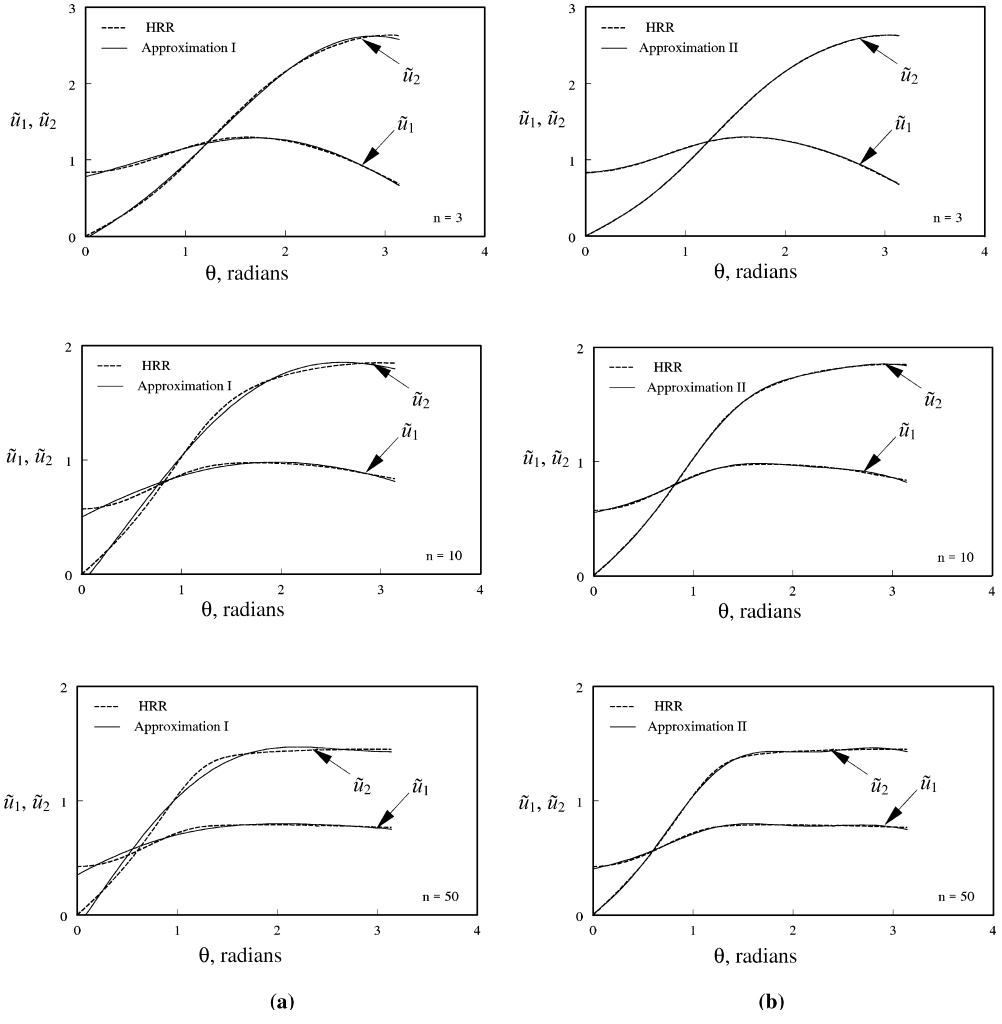

Fig. 2. Approximations of HRR displacement field for plane stress: **a** Approximation I [Eq. (40)], **b** approximation II [Eq. (41)]

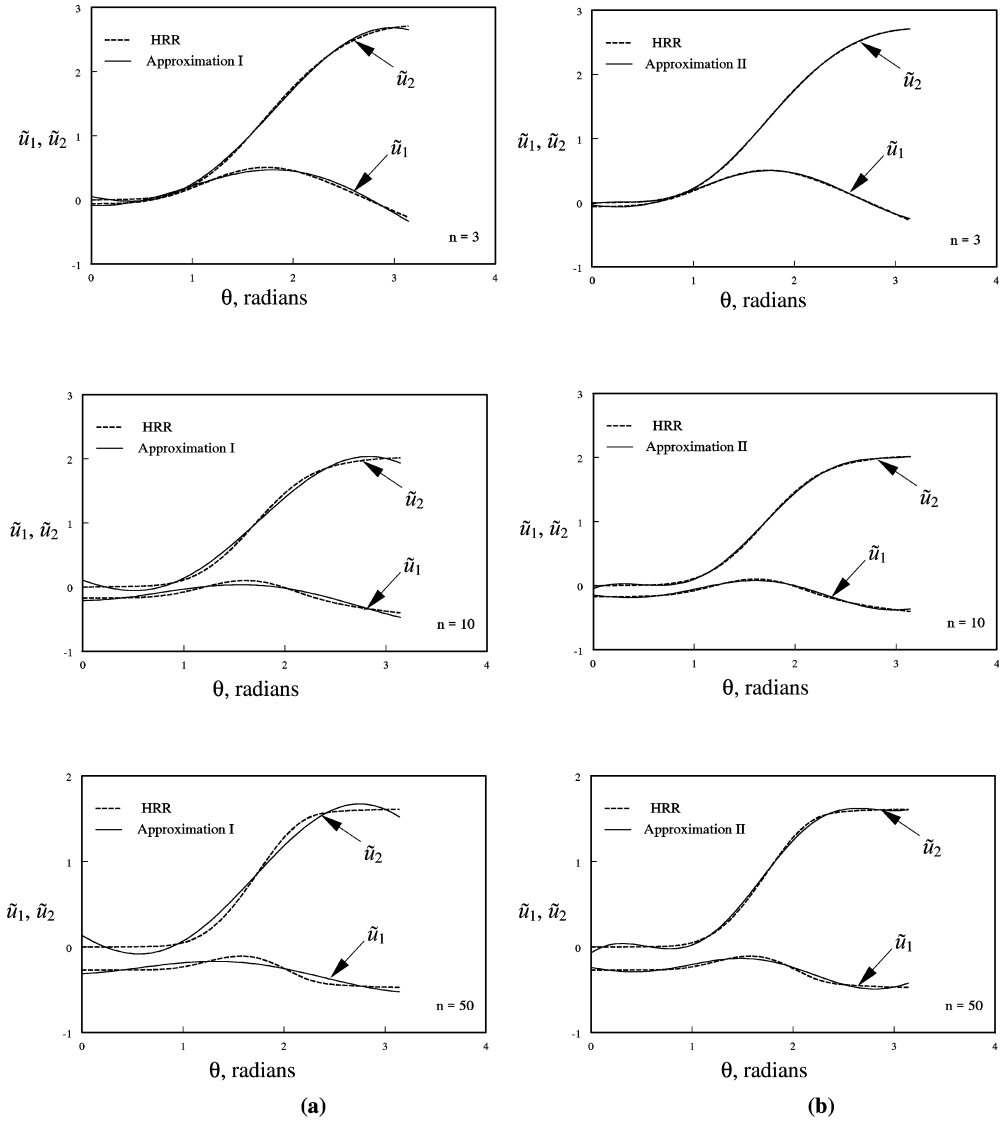

Fig. 3. Approximations of HRR displacement field for plane strain: **a** Approximation I [Eq. (40)], **b** approximation II [Eq. (41)]

and

$$\text{Type II: } \mathbf{p}^T(\mathbf{x}) = \left\{ \begin{array}{l} 1, x_1, x_2, r^{\frac{1}{n+1}}\cos\frac{\theta}{2}, r^{\frac{1}{n+1}} \\ \times \sin\frac{\theta}{2}, r^{\frac{1}{n+1}}\sin\frac{\theta}{2}\sin\theta, r^{\frac{1}{n+1}}\cos\frac{\theta}{2}\sin\theta, \\ r^{\frac{1}{n+1}}\sin\frac{\theta}{2}\sin 3\theta, r^{\frac{1}{n+1}}\cos\frac{\theta}{2}\sin 3\theta \end{array} \right\}. \tag{43}$$

Note, the linear terms in both enriched bases are not related to crack-tip fields, but are needed for linear completeness of EFGM. The Type I enriched basis function in Eq. (42) can be viewed as a generalized enriched basis function, which degenerates to the LEFM basis function (Eq. (39)) when $n = 1$ (linear-elastic). Both types of basis functions have been successfully utilized to predict accurate elastic–plastic crack-tip fields [20].

5
Rates of fracture parameters

5.1
Virtual crack extension

In fracture analysis, the coordinates of all meshless nodes, or any other arbitrary point are measured using the crack tip as the origin, where the x_1 axis is oriented along the direction of the crack length and the x_2 axis is perpendicular to the crack length. When the crack tip is virtually perturbed by a small amount, say $\delta\mathbf{a} = \{\delta a_1, \delta a_2\}^T$ for which δa_1 and δa_2 represent the components of virtual crack extension in the x_1 and x_2 directions, the coordinates of all nodes and any arbitrary point, except the crack-tip node (the reference point), are virtually shifted in the opposite direction by the same amount, as shown in the Fig. 4. In general, $\delta\mathbf{a}$ has two components, δa_1 and δa_2, respectively measured along the crack-length direction and perpendicular to the crack-length direction. The variation of any arbitrary point $\mathbf{x}$ is then

$$\delta\mathbf{x} = \begin{cases} \delta\mathbf{x}_I, & \text{if } \mathbf{x} = \mathbf{x}_I \\ -\delta\mathbf{a}, & \text{otherwise} \end{cases}, \tag{44}$$

where

$$\delta\mathbf{x}_I = \begin{cases} 0, & \text{if } I = \text{crack-tip node} \\ -\delta\mathbf{a}, & \text{if } I \neq \text{crack-tip node} \end{cases}. \tag{45}$$

Note that Eq. (45) is valid only when the crack-tip node is virtually perturbed. If all nodes along the crack length are

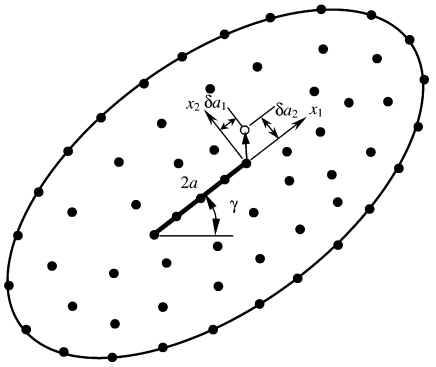

Fig. 4. Meshless discretization and virtual crack extension

virtually perturbed proportionally to their distance from the crack tip, Eq. (45) can be generalized as

$$\delta \mathbf{x}_I = \begin{cases} -\bar{d}_c \delta \mathbf{a}, & \text{if } I \in \text{nodes along crack length} \\ -\delta \mathbf{a}, & \text{if } I \notin \text{nodes along crack length} \end{cases} , \tag{46}$$

where $\bar{d}_c$ is the ratio of the distance between node I and the crack tip to the length of the crack.

5.2
Variations of shape function and its derivatives

Using Eqs. (9) and (10), the variations of the shape function $\Phi_I(\mathbf{x})$ and its partial derivative $\Phi_{I,i}(\mathbf{x})$ are

$$\delta\Phi_I = \delta\mathbf{p}^T\mathbf{A}^{-1}\mathbf{C}_I + \mathbf{p}^T\delta\mathbf{A}^{-1}\mathbf{C}_I + \mathbf{p}^T\mathbf{A}^{-1}\delta\mathbf{C}_I \tag{47}$$

and

$$\begin{aligned}\delta\Phi_{I,i} = {} & \delta\mathbf{p}_{,i}^T\mathbf{A}^{-1}\mathbf{C}_I + \delta\mathbf{p}^T\mathbf{A}_{,i}^{-1}\mathbf{C}_I + \delta\mathbf{p}^T\mathbf{A}^{-1}\mathbf{C}_{I,i} \\ & + \mathbf{p}_{,i}^T\delta\mathbf{A}^{-1}\mathbf{C}_I + \mathbf{p}^T\delta\mathbf{A}_{,i}^{-1}\mathbf{C}_I + \mathbf{p}^T\delta\mathbf{A}^{-1}\mathbf{C}_{I,i} \\ & + \mathbf{p}_{,i}^T\mathbf{A}^{-1}\delta\mathbf{C}_I + \mathbf{p}^T\mathbf{A}_{,i}^{-1}\delta\mathbf{C}_I + \mathbf{p}^T\mathbf{A}^{-1}\delta\mathbf{C}_{I,i}\end{aligned} , \tag{48}$$

where variations $\delta\mathbf{p}$, $\delta\mathbf{p}_{,i}$, $\delta\mathbf{C}_I$, $\delta\mathbf{C}_{I,i}$, $\delta\mathbf{A}$, $\delta\mathbf{A}_{,i}$, δA^{-1}, and $\delta\mathbf{A}_{,i}^{-1}$ can be obtained from the EFGM formulation described in a previous section. See Rao and Rahman [17] for explicit details of these variations.

5.3
Sensitivity of generalized displacement

When the converged solution is reached, Eq. (16) leads to

$$\begin{bmatrix} \mathbf{k}(\mathbf{d}) & \mathbf{G} \\ \mathbf{G}^T & 0 \end{bmatrix} \begin{Bmatrix} \mathbf{d} \\ \mathbf{f}_R \end{Bmatrix} = \begin{Bmatrix} \mathbf{f}^{ext} \\ \mathbf{0} \end{Bmatrix} . \tag{49}$$

Taking the variation on both sides of Eq. (49) yields

$$\begin{bmatrix} \mathbf{k}(\mathbf{d}) & \mathbf{G} \\ \mathbf{G}^T & \mathbf{0} \end{bmatrix} \begin{Bmatrix} \delta\mathbf{d} \\ \delta\mathbf{f}_R \end{Bmatrix} = -\begin{bmatrix} \delta\mathbf{k}(\mathbf{d}) & \delta\mathbf{G} \\ \delta\mathbf{G}^T & \mathbf{0} \end{bmatrix} \begin{Bmatrix} \mathbf{d} \\ \mathbf{f}_R \end{Bmatrix} , \tag{50}$$

which is a linear system of equations with respect to $\delta\mathbf{d}$. Note, the solution of $\delta\mathbf{d}$ can be obtained efficiently, since the same set of linear equations is obtained at the converged state, although a different fictitious load, *i.e.*, the right hand side of Eq. (50), is involved.

Suppose the crack length is virtually perturbed by a small arbitrary value δa in the original direction of the crack length, *i.e.*, $\delta a_1 = \delta a$ and $\delta a_2 = 0$. The derivative of the generalized displacement $\mathbf{d}$ with respect to the crack length a can then be approximated by

$$\frac{\partial \mathbf{d}}{\partial a} \approx \frac{\delta \mathbf{d}}{\delta a} . \tag{51}$$

Equation 51 was used for all numerical calculations presented in forthcoming sections.

Note that by assigning appropriate values of δa_1 and δa_2, similar expressions can be derived to calculate rates of $\mathbf{d}$ with respect to crack length extensions in any direction. For example, if the values of δa_1 and δa_2 are arbitrarily selected, then $\delta\mathbf{d}/\|\delta\mathbf{a}\|$ provides the rate of the generalized displacement with respect to the crack length extension at an angle $\tan^{-1}(\delta a_2/\delta a_1)$ with respect to the direction of the crack length, where $\|\delta\mathbf{a}\| = \sqrt{\delta a_1^2 + \delta a_2^2}$. This issue, however, was not explored in detail during the course of this study.

5.4
Sensitivity of the *J*-integral

The derivative of the J-Integral with respect to crack length a can be calculated from the derivatives of displacement, strain, and stress with respect to a at all meshless nodes. Differentiating both sides of Eq. (27) with respect to a yields

$$\begin{aligned}\frac{\partial J}{\partial a} = {} & \int_A \frac{\partial}{\partial a}\left(\sigma_{ij}\frac{\partial u_i}{\partial x_1} - W\delta_{1j}\right)\frac{\partial q}{\partial x_j}\,\mathrm{d}A \\ & + \int_A \left(\sigma_{ij}\frac{\partial u_i}{\partial x_1} - W\delta_{1j}\right)\frac{\partial}{\partial a}\left(\frac{\partial q}{\partial x_j}\right)\mathrm{d}A .\end{aligned} \tag{52}$$

In Eq. (52), derivatives of stress components σ_{ij} with respect to a can be obtained using the derivatives of generalized displacements and the strain-displacement relation in conjunction with the stress–strain relation. Derivatives of the displacement components u_i with respect to a can be obtained using the derivatives of the generalized displacements and the shape function values of meshless nodes.

6
Probabilistic fracture mechanics and reliability

6.1
Random parameters and fracture response

Consider a mode-I loaded nonlinear-elastic cracked structure under uncertain mechanical and geometric characteristics that is subject to random loads. Denote by $\mathbf{X}$ an N-dimensional random vector with components $X_1, X_2, \ldots, X_N$ characterizing uncertainties in the load, crack geometry, and material properties. For example, if the crack size a, elastic modulus E, far-field applied stress magnitude σ^∞, Ramberg-Osgood parameters α and n, and mode-I fracture toughness at crack initiation J_{Ic} are modeled as random input variables, then $\mathbf{X} = \{a, E, \sigma^\infty, \alpha, n, J_{IC}\}^T$. Let the J-integral (J) be the relevant crack-driving force that can be calculated from nonlinear meshless analysis. Suppose the structure fails when $J > J_{Ic}$. This requirement cannot be satisfied with certainty, because J depends on input vector $\mathbf{X}$, which is random, and J_{Ic} itself is a random variable. Consequently, the performance of the cracked structure should be

evaluated using the reliability P_S, or its complement, the probability of failure $P_F(P_S = 1 - P_F)$, defined as

$$P_F \overset{\text{def}}{=} \Pr[g(\mathbf{X}) < 0] \overset{\text{def}}{=} \int_{g(\mathbf{x})<0} f_{\mathbf{X}}(\mathbf{x})\mathrm{d}\mathbf{x} \,, \tag{53}$$

where $f_{\mathbf{X}}(\mathbf{x})$ is the joint probability density function of $\mathbf{X}$, and

$$g(\mathbf{x}) = J_{Ic}(\mathbf{x}) - J(\mathbf{x}) \tag{54}$$

is the performance function. Note that P_F in Eq. (53) represents the probability of crack-growth initiation and provides a conservative estimate of structural performance. A less conservative evaluation requires calculation of failure probability based on crack-instability criterion. The latter probability is more difficult to compute, since it must be obtained by incorporating crack-growth simulation in a finite element or meshless analysis. However, if suitable approximations of J can be developed analytically, the failure probability due to crack-instability can be easily calculated as well [6, 34].

6.2
Reliability analysis by FORM

The generic expression for the failure probability in Eq. (53), for which the performance function is represented by Eq. (54) involves multi-dimensional probability integration for evaluation. In this study, FORM [35] was used to compute this probability. It is briefly described here to compute the probability of failure P_F in Eq. (53) assuming a generic N -dimensional random vector $\mathbf{X}$ and the performance function $g(\mathbf{x})$ defined by Eq. (54).

The first-order reliability method is based on linear (first–order) approximation of the limit state surface $g(\mathbf{x}) = 0$ tangent to the closest point of the surface to the origin of the space. The determination of this point involves nonlinear constrained optimization and is usually performed in the standard Gaussian image of the original space. The FORM algorithm involves three major steps. First, the space $\mathbf{x}$ of uncertain parameters $\mathbf{X}$ is transformed into a new N-dimensional space $\mathbf{u}$ consisting of independent standard Gaussian variables $\mathbf{U}$. The original limit state $g(\mathbf{x}) = 0$ then becomes mapped into the new limit state $g_U(\mathbf{u}) = 0$ in the $\mathbf{u}$ space. Second, the point on the limit state $g_U(\mathbf{u}) = 0$ having the shortest distance to the origin of the $\mathbf{u}$ space is determined using an appropriate nonlinear optimization algorithm. This point is referred to as the design point, or beta point, and has a distance β_{HL} (known as reliability index) to the origin of the $\mathbf{u}$ space. Third, the limit state $g_U(\mathbf{u}) = 0$ is approximated by a hyperplane $g_L(\mathbf{u}) = 0$, tangent to it at the design point. The probability of failure P_F [Eq. (53)] is thus approximated by $P_{F,1} = \Pr[g_L(\mathbf{u}) < 0]$ in FORM and is given by [35]

$$P_{F,1} \quad = \quad \Phi(-\beta_{HL}) \tag{55}$$

where

$$\Phi(u) = \frac{1}{\sqrt{2\pi}} \int_{-\infty}^{u} \exp\left(-\frac{1}{2}\xi^2\right)\mathrm{d}\xi \tag{56}$$

is the cumulative probability distribution function of a standard Gaussian random variable. A recursive quadratic-programming algorithm [36, 37] was employed to solve the associated optimization problem in this work. The first-order sensitivities were calculated analytically and are described as follows.

6.3
Analytical gradients

In the $\mathbf{u}$ space, the objective function is quadratic; hence, calculating its first-order derivative with respect to u_k , $k = 1,2, \ldots, N$ is trivial. For the constraint function, i.e., the performance function, one must also calculate its derivative with respect to u_k. Assume that a transformation of $\mathbf{x} \in \Re^N$ to $\mathbf{u} \in \Re^N$, given by

$$\mathbf{x} = \mathbf{x}(\mathbf{u}) \ , \tag{57}$$

exists. Hence, the performance function in the $\mathbf{u}$ space can then be written as

$$g_U(\mathbf{u}) = g(\mathbf{x}(\mathbf{u})) = J_{Ic}(\mathbf{x}(\mathbf{u})) - J(\mathbf{x}(\mathbf{u})) \ . \tag{58}$$

Using the chain rule of differentiation, the first-order derivative of with $g_U(\mathbf{u})$ respect to u_k is

$$\frac{\partial g_U(\mathbf{u})}{\partial u_k} = \sum_{j=1}^{N} \frac{\partial g}{\partial x_j}\frac{\partial x_j}{\partial u_k} = \sum_{j=1}^{N} \frac{\partial g}{\partial x_j} R_{jk} \ , \tag{59}$$

where $R_{jk} = \partial x_j / \partial u_k$, which can be obtained from the explicit form of Eq. (57).

In mode-I fracture with $\mathbf{X} = \{a, E, \sigma^{\infty}, \alpha, n, J_{IC}\}^T$, the partial derivatives of g in the $\mathbf{x}$ space can be obtained as

$$\frac{\partial g}{\partial a} = \frac{-\partial J}{\partial a}, \tag{60}$$

$$\frac{\partial g}{\partial E} = -\frac{\partial J}{\partial E} = \frac{J}{E} \quad (\text{since } J \propto 1/E) \ , \tag{61}$$

$$\frac{\partial g}{\partial J_{IC}} = 1 \ . \tag{62}$$

For the partial derivatives of the J-Integral with respect to α and σ^{∞}, it is assumed that the plastic component of J is much larger than the elastic component of J. This is true when the elastic strains are much smaller than the plastic strains, which is characteristic of moderate to high loads in a nonlinear-elastic material. Accordingly,

$$\frac{\partial g}{\partial \alpha} = -\frac{\partial J}{\partial \alpha} = -\frac{J}{\alpha} \tag{63}$$

$$\frac{\partial g}{\partial \sigma^{\infty}} = -\frac{\partial J}{\partial \sigma^{\infty}} = -\frac{(n+1)J}{\sigma^{\infty}} \ . \tag{64}$$

When the assumption above is not valid, the partial derivatives of the J with respect to α and σ^{∞} can no longer be approximated using Eqs. (63) and (64). In this case, size sensitivity analysis method must be applied. If required, the derivative of the J with respect to n can also be calculated by size sensitivity analysis. Size sensitivity analysis, which is simpler than the shape sensitivity analysis developed herein, is not considered in this study.

Using the shape sensitivity formulation presented in a past section, the partial derivative of J with respect to crack size can be easily calculated. For a given $\mathbf{u}$ or $\mathbf{x}$, all

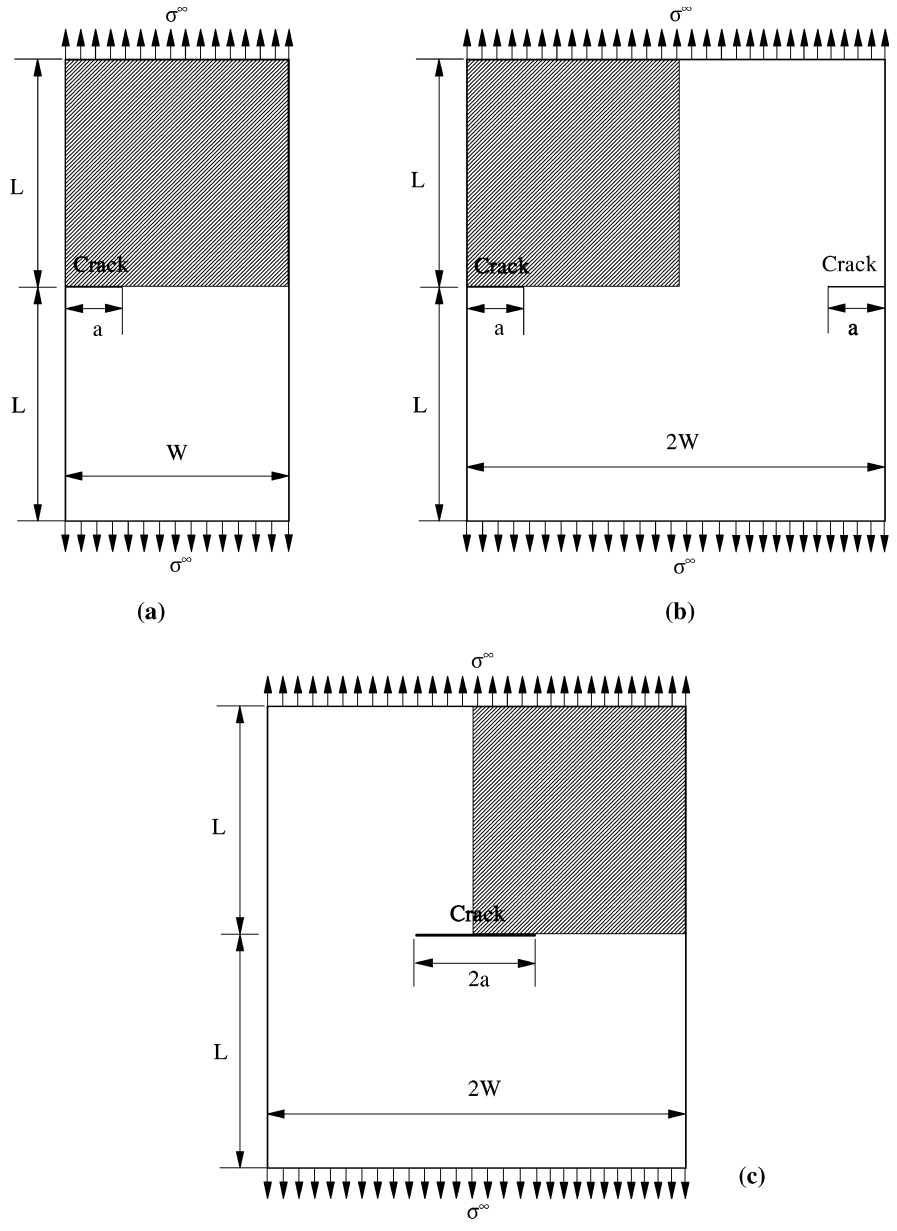

Fig. 5. Fracture specimens under far-field tension: **a** SE(T) specimen, **b** DE(T) specimen and **c** M(T) specimen

gradients of $g_U(\mathbf{u})$ can then be evaluated analytically. FORM or any other gradient-based reliability analysis can therefore be performed efficiently.

7
Numerical examples

Three numerical examples involving mode-I loading conditions are presented in this section. The first example is presented to assess the performance of the nonlinear EFGM formulation for evaluating the elastic-plastic fracture parameters. The next two examples demonstrate the capability of the proposed stochastic meshless method in evaluating the sensitivity and reliability of cracked structures.

7.1
Example 1: *J*-integral evaluations for SE(T), DE(T), and M(T) specimens

Consider three rectangular plates illustrated in Fig. 5a–c, comprising single-edge tension [SE(T)], double-edge tension [DE(T)], and middle tension [M(T)] specimens [25], subjected to a far-field remote tensile stress σ^{∞}. For numerical analysis, values of width $2W = 1.016$ m, length $2L = 5.08$ m, crack length $a = 0.254$ m. The material parameters involved: $E = 206.8$ GPa, $\nu = 0.3$, $\sigma_0 = 154.8$ MPa, $\alpha = 3.8$, and $n = 8.073$.

Due to symmetry, meshless discretizations were performed for only half the plate for the SE(T) specimen, and a quarter of the plate for the DE(T) and M(T) specimens, as depicted by the shaded regions in Fig. 5a–c. The discretization involves 286 regularly distributed nodes, however, in the vicinity of the crack-tip region $Q_1Q_2Q_3Q_4$, [see Fig. 6a] additional 63 nodes were used, as shown in the Fig. 6b, for a total of 349 meshless nodes. A domain of size $2b \times b$, with $b = 0.254$ m, was used to calculate the *J*-integral. The domain of the plate in Fig. 6a was divided by 10×25 rectangular cells with corner points coincident with the 286 meshless nodes, solely for the purpose of numerical integration. An 8×8 Gaussian integration

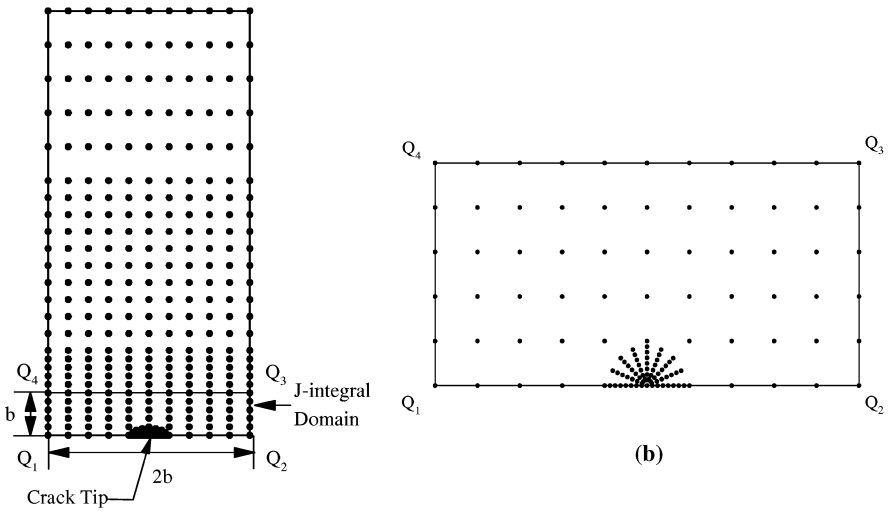

Fig. 6. Meshless discretization of fracture specimens for $a/W = 0.5$: **a** Half (SE(T)) and Quarter (DE(T)) model, **b** Closeup of $Q_1Q_2Q_3Q_4$ region

scheme was employed over the background grid. The weight function parameter $\beta = 3$ was used for meshless analysis. Both plane stress and plane strain conditions were employed.

Figure 7a–c show plots of J-integral versus σ^∞ for the plane stress condition, as predicted by the meshless method for SE(T), DE(T), and M(T) plates, respectively using both Type I and Type II basis functions. A domain form of Eq. (27) was used in calculating the J-integral [15]. Also plotted in the same figures are the corresponding analytical J-integral solutions, which are described in Appendix A. Similar comparisons between meshless and analytical results are shown in Fig. 8a–c for the plane strain condition. In both stress states, the meshless results using proposed basis functions match very well with the analytical solutions for load intensities and material constants considered.

The CPU time required for meshless methods increases with the length of basis functions, because the dimension of the matrix that needs to be inverted for the construction of meshless shape function is directly proportional to the square of the length of basis function. Hence, the CPU time using the Type II enriched basis is slightly higher than that using the Type I enriched basis. This numerical example shows that in terms of accuracy, the performance of the Type I enriched basis function is comparable to the Type II enriched basis function.

7.2
Example 2: sensitivity analysis of M(T) and SE(T) specimens

Consider a middle-tension [M(T)] and a single-edged-tension [SE(T)] specimens with width $2W = 1.016$ m (40 inches), and length $2L = 5.08$ m (200 inches), that are subject to a far-field tensile stress $\sigma^\infty = 172.4$ MPa. Three distinct crack sizes with normalized crack lengths $a/W = 0.3$, 0.4 and 0.5 were considered for both M(T) and SE(T) specimens. The material properties of both specimens were: reference stress $\sigma_0 = 154.8$ MPa; elastic modulus $E = 207$ GPa; Poisson's ratio $\nu = 0.3$; and Ramberg–Osgood parameters $\alpha = 8.073$ and $n = 3.8$. A plane stress condition was assumed.

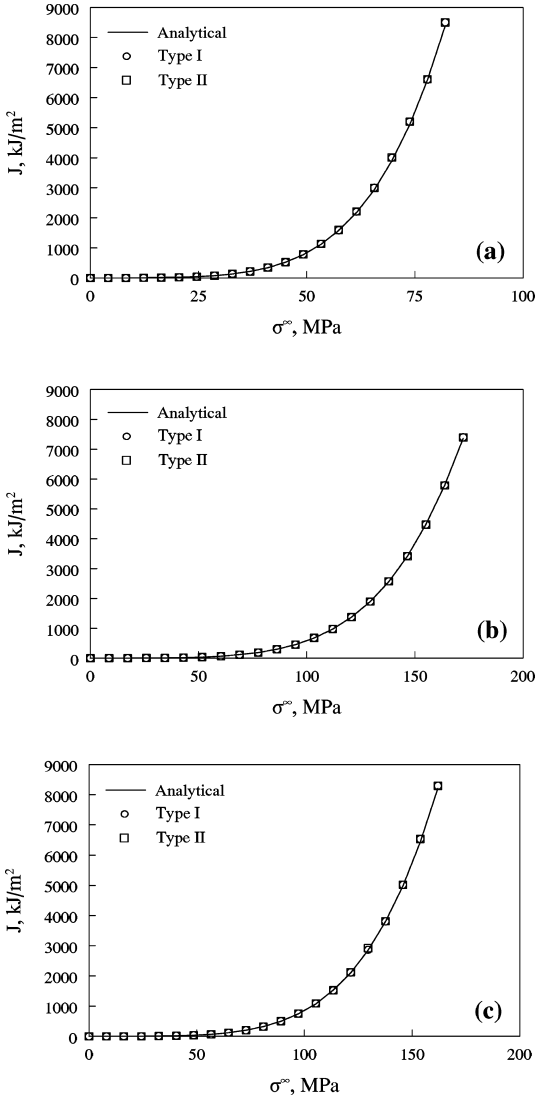

Fig. 7. J-integral versus σ^∞ for all the three specimens under plane stress: **a** SE(T) specimen, **b** DE(T) specimen and **c** M(T) specimen

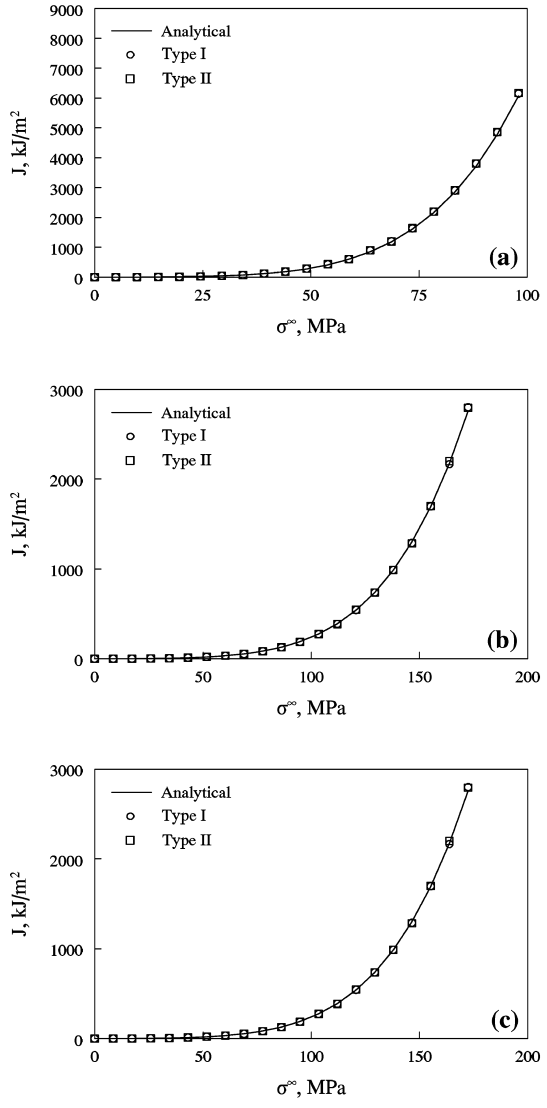

Fig. 8. *J*-integral versus σ^{∞} for all the three specimens under plane strain: **a** SE(T) specimen, **b** DE(T) specimen and **c** M(T) specimen

Figure 5a and c depict geometry and loads of the SE(T) and M(T) specimens, respectively. Due to symmetry, meshless discretization was performed on only a half SE(T) specimen model (single symmetry) and a quarter M(T) specimen model (double-symmetry). Figure 6a shows the meshless discretization for $a/W = 0.5$. The discretization involved 286 regularly distributed nodes, however, in the vicinity of the crack-tip region $Q_1Q_2Q_3Q_4$, [see Fig. 6a] additional 63 nodes were used, as shown in the Fig. 6b, for a total of 349 meshless nodes. The domain of the plate in Fig. 6a was divided by 10×25 rectangular cells with corner points coincident with the 286 meshless nodes, solely for the purpose of numerical integration. A domain of size $2b \times b$, where $b = \min\{a, (W - a)\}$, was used to calculate the *J*-integral. An 8×8 Gaussian integration scheme was employed over the background grid. The enriched basis function described by Eq. (42) and weight function parameter $\beta = 3$ were used for meshless analysis.

Tables 1 and 2 present, respectively, the predicted results of J and $\partial J/\partial a$ for the M(T) and SE(T) specimens, respectively. Two sets of results are shown. One involves the proposed nonlinear meshless method and the virtual crack extension method for sensitivity analysis. The other entails nonlinear finite element method using the ABAQUS commercial code [38] and finite-difference method for sensitivity analysis. A one-percent perturbation of crack length was employed in the finite-difference method. The results in Tables 1 and 2 show that the proposed meshless method provides reasonably accurate estimates for $\partial J/\partial a$ in comparison with the corresponding results of the finite-difference method. The maximum difference between the results of the proposed method and the finite-difference method is about three percent.

7.3
Example 3: reliability analysis of DE(T) specimen

Consider a double-edge tension [DE(T)] specimen with width $2W$ = 1.016 m (40 inches), length $2L$ = 5.08 m (200 inches), and crack length a = 0.254 m (10 inches), as shown in Fig. 5b. The specimen is subject to a far-field

Table 1. Sensitivity of *J* for M(T) specimen by the proposed and finite difference methods

a/W	*J*-Integral *J*, kJ/m^2			Sensitivity of *J*-Integral d*J*/d*a*, kJ/m^3		
	Proposed method	FEM	Difference percent	Proposed method	Finite difference	Difference percent
0.3	2.6×10^3	2.7×10^3	+3.70	36.5×10^3	35.8×10^3	−1.95
0.4	5.1×10^3	5.1×10^3	0.0	70.9×10^3	69.64×10^3	−1.81
0.5	10.9×10^3	11.2×10^3	+2.68	18.1×10^4	17.6×10^4	−2.84

Table 2. Sensitivity of *J* for SE(T) specimen by the proposed and finite difference methods

a/W	*J*-Integral *J*, kJ/m^2			Sensitivity of *J*-Integral d*J*/d*a*, kJ/m^3		
	Proposed method	FEM	Difference percent	Proposed method	Finite difference	Difference percent
0.3	1.1×10^4	1.1×10^4	0.00	29.2×10^4	30.2×10^4	+3.31
0.4	5.4×10^4	5.2×10^4	−3.85	18.5×10^5	18.1×10^5	−2.21
0.5	3.6×10^5	3.7×10^5	+2.70	17.6×10^6	16.8×10^6	−2.38

Table 3. Statistical properties of random input for DE(T) specimen

Random Variable	Mean	COV[a]	Probability distribution
Normalized crack length (a/W)	0.5	Variable[b]	Lognormal
Elastic modulus (E)	207 GPa	0.05	Gaussian
Yield offset (α)	8.073	0.1439	Gaussian
Initiation fracture toughness (J_{Ic})	1243 kJ/m^2	0.47	Lognormal
Far-field tensile stress (σ^{∞})	Variable[b]	0.1	Gaussian

[a] Coefficient of variation (COV) = standard deviation/mean
[b] Arbitrarily varied

tensile stress σ^{∞}. The load σ^{∞}, crack size a/W, and material properties E, α and J_{Ic} were treated as statistically independent random variables. Table 3 lists the means, coefficients of variation (COV), and probability distributions of these random parameters. The Poisson's ratio $\nu = 0.3$, and the Ramberg–Osgood exponent $n = 3.8$ were assumed to be deterministic. A plane stress condition was assumed.

Due to symmetry, meshless discretization was performed on only one-fourth of the model, as shown in Fig. 6a. The discretization involves 286 regularly distributed nodes, however, in the vicinity of the crack-tip region $Q_1Q_2Q_3Q_4$, [see Fig. 6a] additional 63 nodes were used, as shown in the Fig. 6b, for a total of 349 meshless nodes. The domain of the plate was divided by 10×25 rectangular cells with corner points coincident with the 286 meshless nodes, solely for the purpose of numerical integration. A domain of size $2b \times b$, where $b = \min\{a, (W - a)\}$, was used to calculate the J-integral. An 8×8 Gaussian integration scheme was employed over the background grid. The enriched basis function described by Eq. (42) and weight function parameter $\beta = 3$ were used for meshless analysis.

A number of probabilistic analyses based on meshless methods were performed to calculate the probability of failure P_F as a function of the mean far-field tensile stress $\mathrm{E}[\sigma^{\infty}]$, in which $\mathrm{E}[\cdot]$ is the expectation (mean) operator. Figure 9 shows the results in the form of P_F vs. $\mathrm{E}[\sigma^{\infty}]$ plots for $v_{a/W} = 10$ percent, where $v_{a/W}$ is the COV of the normalized crack length a/W. The probability of failure was calculated using both meshless-based FORM and FEM-based Monte Carlo simulation. For FORM, the proposed virtual crack extension method was used to obtain sensitivities of J. For the simulation method, the sample size was 10,000. Figure 9 demonstrates good agreement between the FORM-based probability of failure and the simulation results.

Using meshless-based FORM, Figure 10 plots P_F vs. $\mathrm{E}[\sigma^{\infty}]$ for both deterministic ($v_{a/W} = 0$) and random ($v_{a/W}$ = 10 and 20 percent) crack sizes. As expected, the results indicate that the failure probability increases with the COV (uncertainty) of a/W. The failure probability can be much larger than the probabilities calculated for a deterministic crack size, particularly when the uncertainty of a/W is large. Figure 10 also contains results of FEM-based FORM involving continuum shape sensitivity analysis [39]. Failure probabilities predicted using the proposed meshless method match very well with those obtained by FEM.

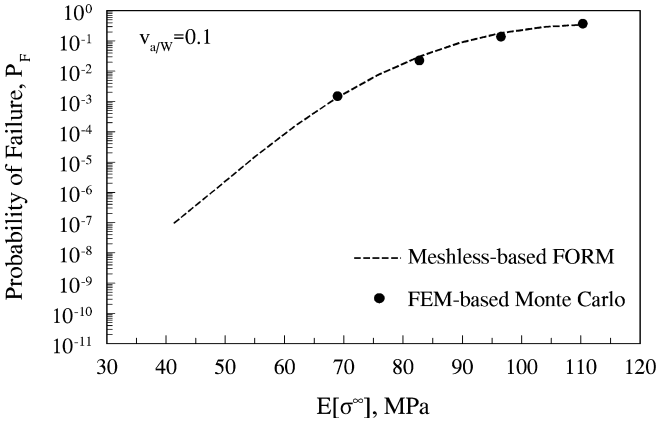

Fig. 9. Failure probability of DE(T) specimen by FORM and simulation

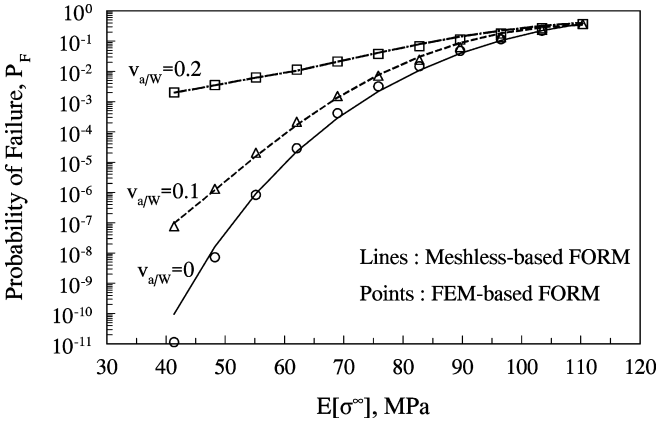

Fig. 10. Failure probability of DE(T) specimen by FORM for various uncertainties in crack size

8 Conclusions

A stochastic meshless method was developed for probabilistic fracture-mechanics analysis of nonlinear cracked structures. The method involves enriched element-free Galerkin formulation for calculating the J-integral; statistical models of uncertainties in load, material properties, and crack geometry; and the first-order reliability method (FORM) for predicting probabilistic fracture response and reliability of cracked structures. The sensitivity of fracture parameters with respect to crack size, required for probabilistic analysis, is calculated using a virtual crack extension technique. Numerical examples based on mode-I fracture problems have been presented to illustrate the

proposed method. The results from sensitivity analysis indicate that the maximum difference between sensitivity of the *J*-integral calculated using the proposed method and reference solutions obtained by the finite-difference method is about three percent. The results from reliability analysis show that the probability of fracture initiation using the proposed sensitivity and meshless-based FORM are very accurate when compared with either the finite-element-based Monte Carlo simulation or finite-element-based FORM. Since all gradients are calculated analytically, the reliability analysis of cracks can be performed efficiently using meshless methods.

Appendix A

J-integral for SE(T), DE(T), and M(T) specimens

Consider SE(T), DE(T), and M(T) specimens subjected to quasi-static far-field tension stress σ^{∞}. The geometrical parameters of these specimens are defined in Fig. 5a–c. The total *J*-integral can be obtained from

$$J = J_e + J_p \tag{65}$$

where J_e and J_p are the elastic and plastic solutions, respectively, and are defined as follows.

A.1 SE(T) specimen [25]

The elastic *J* is

$$J_e = \frac{\sigma^{\infty^2}\pi a}{E'}\left[0.265(1-a/W)^4 + (0.857+0.265\,a/W)/(1-a/W)^{1.5}\right]^2 . \tag{66}$$

The plastic *J* is

$$J_p = \frac{\alpha\sigma_0^2}{E}(W-a)h_1(a/W,n)\left(\frac{P}{P_0}\right)^{n+1} , \tag{67}$$

where $P = \sigma^{\infty}WB$ is the far-field tensile load,

$$P_0 = \begin{cases} 1.072\eta B(a-W)\sigma_0, & \text{plane stress} \\ 1.455\eta B(a-W)\sigma_0, & \text{plane strain} \end{cases} \tag{68}$$

is the reference load, and $h_1(a/W,n)$ is a dimensionless plastic influence function that are tabulated in Ref. [25].

A.2 DE(T) specimen [25]

The elastic *J* is

$$J_e = \frac{\sigma^{\infty^2}\pi a}{E'}\left[1.12+0.2(a/W)-1.2(a/W)^2 + 1.93(a/W)^3\right]^2 . \tag{69}$$

The plastic *J* is

$$J_p = \frac{\alpha\sigma_0^2}{E}(W-a)h_1(a/W,n)\left(\frac{P}{P_0}\right)^{n+1} , \tag{70}$$

where $P = \sigma^{\infty}2WB$ is the far-field tensile load,

$$P_0 = \begin{cases} \frac{4}{\sqrt{3}}\sigma_0(W-a)B, & \text{plane stress} \\ \left[0.72+1.82\left(1-\frac{a}{W}\right)\right]\sigma_0 WB, & \text{plane strain} \end{cases} \tag{71}$$

is the reference load, and $h_1(a/W,n)$ is a dimensionless plastic influence function that are tabulated in Ref. [25].

A.3 M(T) specimen [25]

The elastic *J* is

$$J_e = \frac{\sigma^{\infty^2}\pi a}{E'}\left[1+0.128a/W-0.288(a/W)^2 + 1.525(a/W)^3\right]^2 . \tag{72}$$

The plastic *J* is

$$J_p = \frac{\alpha\sigma_0^2}{E}(W-a)h_1(a/W,n)\left(\frac{P}{P_0}\right)^{n+1} , \tag{73}$$

where $P = \sigma^{\infty}2WB$ is the far-field tensile load,

$$P_0 = \begin{cases} 2B(a-W)\sigma_0, & \text{plane stress} \\ \frac{4}{\sqrt{3}}B(a-W)\sigma_0, & \text{plane strain} \end{cases} \tag{74}$$

is the reference load, and $h_1(a/W,n)$ is a dimensionless plastic influence function that are tabulated in Ref. [25].

In Eqs. (68), (71), and (74),

$$E' = \begin{cases} E, & \text{plane stress} \\ \frac{E}{1-\nu^2}, & \text{plane strain} \end{cases} \tag{75}$$

is the effective modulus of elasticity, and ν is the Poisson's ratio.

References

1. **Provan JW** (1987) Probabilistic Fracture Mechanics and Reliability. Martinus Nijhoff Publishers, Dordrecht, The Netherlands
2. **Grigoriu M, Saif MTA, El-Borgi S, Ingraffea A** (1990) Mixed-mode fracture initiation and trajectory prediction under random stresses. Int. J. Fracture 45: 19–34
3. **Besterfield GH, Liu WK, Lawrence MA, Belytschko T** (1991) Fatigue crack growth reliability by probabilistic finite elements. Comput. Meth. Appl. Mech. Eng. 86: 297–320
4. **Besterfield GH, Lawrence MA, Belytschko T** (1990) Brittle fracture reliability by probabilistic finite elements. ASCE J. Eng. Mech. 116(3): 642–659
5. **Rahman S** (2001) Probabilistic fracture mechanics: *J*-estimation and finite element methods. Eng. Fracture Mech. 68: 107–125
6. **Rahman S, Kim J-S** (2001) Probabilistic fracture mechanics for nonlinear structures. Int. J. Pressure Vessels and Piping 78(4): 261–269
7. **Rahman S** (1995) A stochastic model for elastic–plastic fracture analysis of circumferential through-wall-cracked pipes subject to bending. Eng. Fracture Mech. 52(2): 265–288
8. **Dillstrom P** (2000) ProSINTAP – A probabilistic program implementing the SINTAP assessment procedure. Eng. Fracture Mech. 67: 647–668
9. **Rahman S, Chen G, Firmature R** (2000) Probabilistic analysis of off-center cracks in cylindrical structures. Int. J. Pressure Vessels and Piping 77(1): 3–16
10. **Belytschko T, Lu YY, Gu L** (1995) Crack propagation by element-free Galerkin methods. Eng. Fracture Mech. 51(2): 295–315
11. **Belytschko T, Tabbara M** (1996) Dynamic fracture using element-free Galerkin methods. Int. J. Numer. Meth. Eng. 39: 923–938
12. **Fleming M, Chu YA, Moran B, Belytschko T, Lu YY, Gu L** (1997) Enriched element-free Galerkin methods for crack-tip fields. Int. J. Numer. Meth. Eng. 40: 1483–1504

13. **Sukumar N, Moran B, Belytschko T** (1998) The natural element method in solid mechanics. Int. J. Numer. Meth. Eng. 43: 839–887
14. **Kaljevic I, Saigal S** (1997) An improved element free Galerkin formulation. Int. J. Numer. Meth. Eng. 40: 2953–2974
15. **Rao BN, Rahman S** (2000) An efficient meshless method for fracture analysis of cracks. Comput. Mech. 26: 398–408
16. **Rao BN, Rahman S** (2001) A coupled meshless-finite element method for fracture analysis of cracks. Int. J. Pressure Vessels and Piping 78(9): 647–657
17. **Rao BN, Rahman S** (2002) Probabilistic fracture mechanics by Galerkin meshless methods – Part I: rates of stress-intensity factors. Comput. Mech. 28(5): 351–364
18. **Rahman S, Rao BN** (2002) Probabilistic fracture mechanics by Galerkin meshless methods – Part II: reliability analysis. Comput. Mech. 28(5): 365–374
19. **Rao BN, Rahman S** (2003) Meshfree analysis of cracks in isotropic functionally graded materials. Eng. Fracture Mech. 70(1): 1–27
20. **Rao BN, Rahman S** (2002) An enriched meshless method for nonlinear fracture mechanics. Proceedings of 2002 ASME Pressure Vessels and Piping Conference, Vancouver, BC, Canada, (also submitted to International Journal for Numerical Methods in Engineering)
21. **Hutchinson JW** (1968) Singular behavior at the end of a tensile crack in a hardening material. J. Mech. Phys. Solids 16: 13–31
22. **Rice JR, Rosengren GF** (1968) Plane strain deformation near a crack tip in a power hardening material. J. Mech. Phys. Solids 16: 1–13
23. **Lancaster P, Salkauskas K** (1981) Surfaces generated by moving least squares methods. Mathematics of Computation 37: 141–158
24. **Chen JS, Wang HP** (2000) New boundary condition treatments in meshfree computation of contact problems. Computer Meth. Appl. Mech. Eng. 187(3–4): 441–468
25. **Anderson TL** (1995) Fracture mechanics: fundamentals and applications. 2nd Edition, CRC Press
26. **Hutchinson JW** (1968) Singular behavior at the end of a tensile crack in a hardening material. J. Mech. Phys. Solids 16: 13–31
27. **Rice JR, Rosengren GF** (1968) Plane strain deformation near a crack tip in a power hardening material. J. Mech. Phys. Solids 16: 1–13
28. **Pan J, Shih CF** (1992) Elastic–plastic analysis of combined mode I, II and III crack-tip fields under small-scale yielding conditions. Int. J. Solids and Struct. 29: 2795–2814
29. **Betegon C, Hancock JW** (1991) Two-parameter characterization of elastic–plastic crack fields. J. Appl. Mech. 58: 104–113
30. **Parks DM** (1992) Advances in characterization of elastic–plastic crack-tip fields. Topics in Fracture and Fatigue, Springer-Verlag, New York
31. **O'Dowd NP, Shih CF** (1991) Family of crack-tip fields characterized by a triaxiality parameter: Part I – structure of fields. J. Mech. Phys. Solids 39(8): 989–1015
32. **O'Dowd NP, Shih CF** (1992) Family of crack-tip fields characterized by a triaxiality parameter: Part I – fracture applications. J. Mech. Phys. Solids 40(8): 939–963
33. **Shih CF** (1983) Tables of Hutchinson–Rice–Rosengren singular field quantities. MRL E-147, Materials Research Laboratory, Brown University
34. **Rahman S, Ghadiali N, Paul D, Wilkowski G** (1995) Probabilistic pipe fracture evaluations for leak-rate-detection applications. NUREG/CR-6004, US Nuclear Regulatory Commission, Washington, DC
35. **Madsen HO, Krenk S, Lind NC** (1986) Methods of structural safety. Prentice-Hall, Inc., Englewood Cliffs, New Jersey
36. **Lim OK, Arora JS** (1986) An active set RQP algorithm for optimum design. Comput. Meth. Appl. Mech. Eng. 57: 51–65
37. **Arora JS** (1989) Introduction to optimum design. McGraw-Hill, New York
38. **ABAQUS** (2002) User's guide and theoretical manual, Version 6.1, Hibbitt, Karlsson, and Sorenson, Inc., Pawtucket, Rhode Island
39. **Chen G, Rahman S** (2001) Shape sensitivity and reliability analyses in nonlinear fracture mechanics. Proceedings of 10th International Congress on Fracture, Honolulu, Hawaii